

Stress inversion in a gelatin box: testing eruptive vent location forecasts with analog models

Lorenzo Mantiloni¹, Timothy John Davis², Ayleen Barbara Gaete Rojas³, and Eleonora Rivalta⁴

¹Helmholtz-Zentrum Potsdam - Deutsches Geoforschungszentrum

²GFZ

³GFZ German Research Centre for Geosciences

⁴Deutsches GeoForschungsZentrum GFZ

November 22, 2022

Abstract

Assessing volcanic hazard in regions of distributed volcanism is challenging because of the uncertain location of future vents. A statistical-mechanical strategy to forecast future vent locations was recently proposed. Here we further develop and test that strategy with analog models. We stress a gelatin block in controlled conditions and observe air-filled crack trajectories. We use the observed surface arrivals to sample the distributions of parameters describing the stress state of the gelatin block, combining deterministic crack trajectory simulations with a Monte Carlo approach. We find the algorithm retrieves the stress imposed on the gelatin and successfully forecasts the arrival points of subsequent cracks in the same experimental setups. We discuss how the approach may be used to gain insight on the stress state of regions of distributed volcanism.

Stress inversion in a gelatin box: testing eruptive vent location forecasts with analog models

L. Mantiloni ^{1,2}, T. Davis ^{1,2}, A.B. Gaete Rojas ¹, E. Rivalta ¹

¹GFZ German Research Centre for Geosciences, Physics of Earthquakes and Volcanoes, Telegrafenberg,
14473 Potsdam, Germany. {lorenzo,davis,agaete,rivalta}@gfz-potsdam.de

²University of Potsdam, Potsdam, Germany

Key Points:

- We stress a gelatin block by excavating its surface and imposing lateral strain, then observe air-filled cracks trajectories
- We numerically simulate the crack trajectories and retrieve the stress state of the gelatin through a Monte Carlo approach
- By combining numerical simulations and posterior distributions of stress parameters we forecast new crack arrivals at the surface

Abstract

Assessing volcanic hazard in regions of distributed volcanism is challenging because of the uncertain location of future vents. A statistical-mechanical strategy to forecast future vent locations was recently proposed. Here we further develop and test that strategy with analog models. We stress a gelatin block in controlled conditions and observe air-filled crack trajectories. We use the observed surface arrivals to sample the distributions of parameters describing the stress state of the gelatin block, combining deterministic crack trajectory simulations with a Monte Carlo approach. We find the algorithm retrieves the stress imposed on the gelatin and successfully forecasts the arrival points of subsequent cracks in the same experimental setups. We discuss how the approach may be used to gain insight on the stress state of regions of distributed volcanism.

Plain Language Summary

In regions of distributed volcanism eruption locations (vents) are scattered over a large area. Forecasting the new eruption locations over such regions is critically important, as many are densely populated. One of the main difficulties is dealing with few known past eruptions, that is, the data available to constrain forecast models are scarce. Here we develop a forecast strategy by using analog models. We observe the propagation of air-filled cracks inside a block of gelatin, which we had previously stressed by applying extension or compression and surface excavations. Such models, if properly scaled, are an analog for magma propagation in the Earth's crust. We use the surface arrival points of some observed cracks to retrieve the statistical distributions of a few parameters controlling the stress field. Next, we use such distributions to simulate many cracks to forecast other observed arrivals. Our strategy may help retrieving the state of stress in volcanic regions and forecast the location of future vents.

1 Introduction

In many volcanic regions, especially monogenetic fields, continental rifts and calderas but also shield volcanoes and stratocones, eruptive vents may be spatially scattered: they sometimes cluster along rift zones or are distributed over areas that may exceed 10,000 km². Some of these regions are densely populated. In order to better protect human life and infrastructure, it is important to better understand the factors determining vent distributions and improve vent location forecasts.

The most common approaches to probabilistic forecasts of future vent opening locations rely on the spatial density of past eruptive events, sometimes complemented with the surface distribution of structural features, such as faults and fractures (Connor & Hill, 1995; Martin et al., 2004; Selva et al., 2012; Bevilacqua et al., 2015). Models based on these approaches, however, often remain poorly constrained due to scarce or spatially sparse data, and cannot be easily validated in volcanic systems where eruptions are infrequent.

Recently, Rivalta et al. (2019) proposed a mechanical-statistical approach to inversely constrain the state of stress, and thus magma pathways, of a volcanic edifice or region on the base of the known location of magma reservoirs and past eruptive vents. Dike trajectories are assumed to follow a "least resistance to opening" path calculated from the elastic stress field, as explained in detail below, and seeks to optimize the stress field so that any magma batch released from the magma reservoir reaches one of the past eruptive vents. Once the stress field is constrained, the trajectories of future dikes can be forecast. Rivalta et al. (2019) adapted and applied the concept only to Campi Flegrei caldera in Italy. Further developments and applications are necessary to harness the potential of the method.

Analog laboratory experiments involving fluid-filled crack propagation in gelatin have proven useful in validating dike propagation models (Watanabe et al., 2002; Maccaferri et al., 2019), also assessing the influence of surface loads (Muller et al., 2001; Gaete et al., 2019), rigidity layering (Maccaferri et al., 2010) and external stress fields (Acocella & Tibaldi, 2005).

Here we further explore the potential of stress inversions to forecast dike trajectories using analog experiments with an imposed stress field, then discuss its performance and relevance for natural systems.

2 Methods

The scheme presented here consists of three main steps. First, we run a series of experiments where we track the propagation of injected air-filled cracks. Second, we use a boundary element (BE) model to calculate expected crack trajectories, combined with a Markov Chain Monte Carlo (MCMC) algorithm to sample two parameters describing the state of stress within the gelatin. Third, we validate our strategy by running forecasts for additional cracks, which we compare to further injections.

2.1 Experimental Setup

We use a perspex container of size $A = 40$ cm, $B = 20$ cm, $C = 30$ cm (fig. 1a). A 2.0 wt% or 2.5 wt% aqueous solution of 220 Bloom pig gelatin powder was let solidify in the box at $T = 8^\circ$ C for 20 h. The gelatin density is assumed to be $\rho_{gel} = 1020$ kg·m⁻³, as measured by Smittarello (2019) on a similar setup for the same gelatin brand and concentrations. Compression or extension were imposed on the set gelatin by inserting or removing two plastic plates of thickness $d^{exp} = 2.5 \pm 0.1$ mm at the box sides, separated from the medium by a transparent plastic film (fig. 1a). The gelatin block surface is moulded to include along the y direction a rectangular, rift-like excavation of width $w = 7$ cm and varying depth h^{exp} (fig. 1a), creating surface unload. Air is injected into the gelatin from the bottom of the box through syringes, resulting in ascending air-filled cracks. Their trajectories are recorded, and the start and surface arrival points of the cracks (x_i^{start} and x_i^{obs} , respectively) are measured (fig. 1c,d).

All experiments were carried out at room temperature, with timescales short enough (≤ 1 h) to maintain the experiments in an elastic regime (Kavanagh et al., 2013). The Young’s modulus E of the gelatin was determined case by case by applying a small cylindrical load on the surface and measuring the resultant subsidence under the assumption of a half space (Kavanagh et al., 2013). Deviations from the analytical solution due to the box walls can be neglected if the load is small enough (Smittarello, 2019). E was mostly within the 2000–3500 Pa range (table 1). We assumed a $\nu = 0.49$ Poisson’s ratio (van Otterloo & Cruden, 2016).

To compute the scaling between our experiments and nature, we consider calderas or rifts of 5 to 25 km diameter or width as the reference cases. The length scaling factor $L^* = 1.4 \cdot 10^{-5} - 2.8 \cdot 10^{-6}$, where the asterisk refers to the ratio between analog and natural values, is thus obtained by dividing w by the assumed width in nature. Another length scale relevant to our experiments is the buoyancy length (Nakashima, 1993):

$$L_b = \left(\frac{K_c}{\pi^{\frac{1}{2}} \Delta \rho g} \right)^{\frac{2}{3}} \quad (1)$$

where K_c is the medium fracture toughness and $\Delta \rho$ is the density contrast between the host medium and the injected fluid. Assuming $\Delta \rho_r = 100$ kg·m⁻³, $\Delta \rho_{gel} = 1000$ kg·m⁻³ as the rock-magma and gelatin-air density contrasts, respectively, and $K_c^r = 0.2 - 1 \cdot 10^9$ Pa·m^{1/2}, $K_c^{gel} = 50 - 80$ Pa·m^{1/2} as the rock and gelatin fracture toughness, respectively, for a gelatin Young’s modulus in the order of $E = 3000$ Pa (Menand & Tait, 2001),

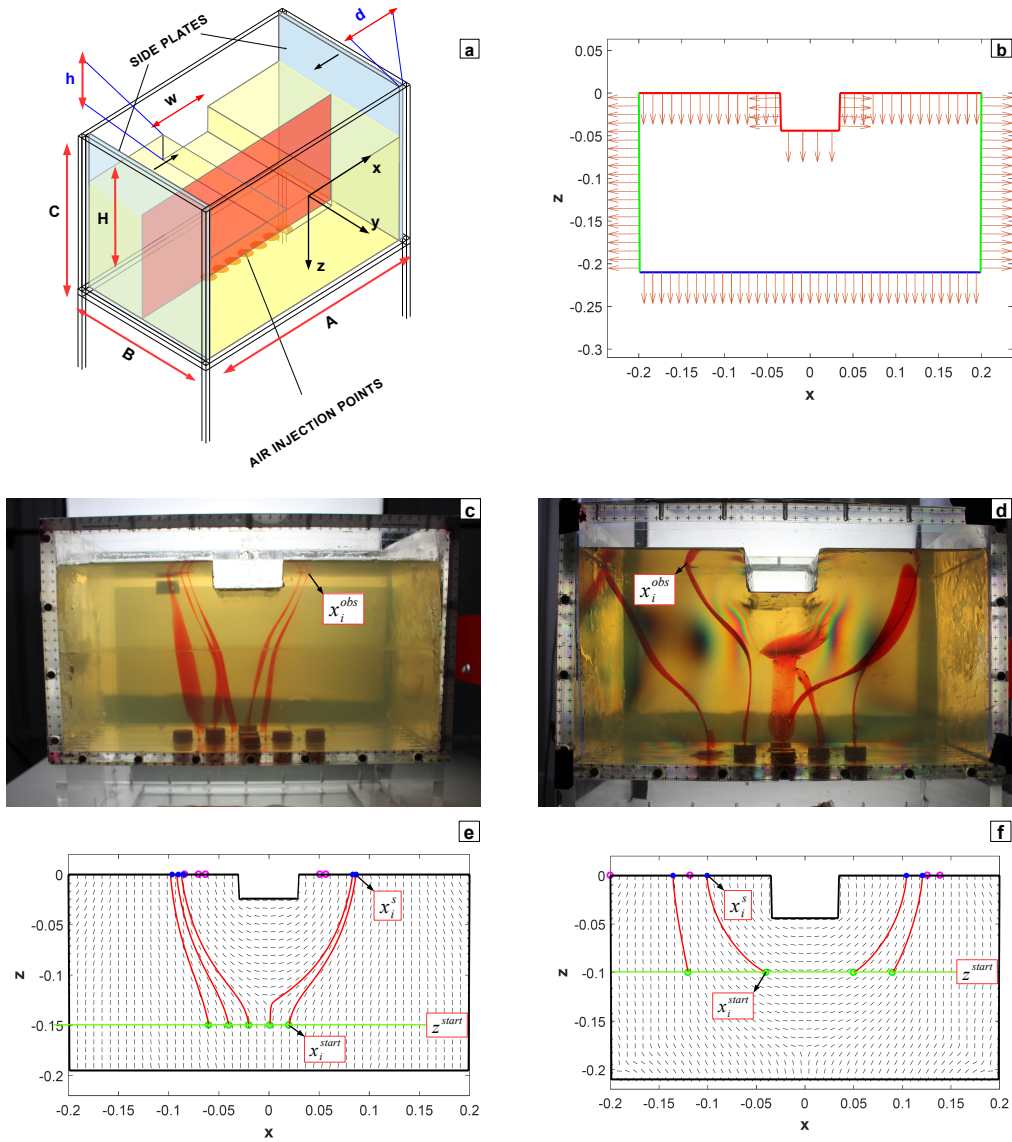


Figure 1. **a** Schematic view of the gelatin box: the side plates are highlighted in blue. The median plane of the block is highlighted in red. **b** Discretization of the box and its surface over the median plane: the normals to the boundary elements are shown as arrows. The length of the illustrated BEs is larger than the one employed in the models. **c** Front view of the gelatin box at the conclusion of experiment 2DLA-4 (extension and layered medium): crack trajectories are marked with red ink. The layer interface is visible as a change in the shade of yellow. **d** Same as in **c**, experiment 2DLA-2 (compression). **e** Numerical simulation of the experiment in **c**): blue dots represent the x_i^s simulated from a random set of parameters, while x_i^{obs} are marked with magenta circles. Simulated trajectories are highlighted in red and the σ_1 directions are drawn in black. z^{start} is marked by a green line. **f** Same as in **e** for the experimental set in **d**.

we obtain $L_b^* = 1.3 \cdot 10^{-5} - -2.9 \cdot 10^{-6}$, comparable with L^* . A typical $z^{start} = -150$ mm (table 1) corresponds to $z^{start} = -10 - -50$ km in nature. Such a starting depth for dikes is rather deep, but not unreasonable.

The stress scaling factor is calculated by dividing the unload stress $\sigma_U = \rho_{gel}gh$ for the excavation in the gelatin by the one for the natural case. Taking $h = 2 - 5$ cm (table 1) and caldera or rift depths in the range 0.3 - 1 km, assuming $\rho_r = 2500 \text{ kg}\cdot\text{m}^{-3}$, we obtain $\sigma^* = 8.2 \cdot 10^{-6} - 6.8 \cdot 10^{-5}$. We also require the ratio between the stress arising from lateral strain and the unloading one to be comparable to natural cases. In our experiments, such ratio $Ee/\rho_{gel}gh$ is in the range 0.06–0.19. The same ratio for Campi Flegrei caldera is ~ 0.26 (Rivalta et al., 2019), which is lower than, but in the same order of magnitude of, our upper limit.

Inhomogeneities of various nature affect the outcome of the experiments. Some of them are unplanned, such as temperature gradients within the gelatin block and localised strain concentrations induced when removing and, especially, inserting the side plates. Conversely, rigidity layering is intentionally introduced in experiments 2DLA-3 & 2DLA-4 (table 1). In this particular experiment series any inhomogeneity is welcome, as it offers a chance of testing the method against medium variability.

2.2 Experimental Data

We carried out a total of ten experiments (2DLA-i, $i=1, \dots, 10$), considering extension (6 experiments), compression (4 experiments), layering (2 experiments) and evolving states of stress (3 experiments).

In experiments 2DLA-1,3,4,5,6,7 we applied extension. 2DLA-3 and 2DLA-4 were performed in layered gelatin. In 2DLA-3, the bottom layer had a higher gelatin concentration, and thus rigidity, than the top one, and reverse in 2DLA-4. For these two experiments we use an “effective” Young’s modulus obtained by carrying out the measurement on the whole block.

In 2DLA-5,6,7 we changed the state of stress midway in the experiments after a first set of injections. In 2DLA-5 we performed 3 injections, then removed the side plates and finally injected 3 more cracks. In 2DLA-6 and 2DLA-7 we partially refilled the surface excavation with water between a first and a second set of injections; the data of these two experiments were then pooled with the purpose of checking the performance of the method with a larger data set. As h^{exp} and E were similar but not identical in the two experiments, we assumed average values.

In experiments 2DLA-2,8,9,10 we imposed compression. These experiments displayed a relatively large variability in the propagation and orientation of the cracks for similar sets of parameters and starting points: observed trajectories diverged significantly from each other, resulting in the cracks hitting the box walls in 2DLA-8, 2DLA-9 and 2DLA-10 or, in one case (2DLA-2), becoming stuck beneath the unload as a sill-like intrusion (fig. 1d). In 2DLA-2 we discarded that one crack, while experiments 2DLA-8,-9 and -10 were discarded entirely, as very few cracks reached the gelatin surface.

2.3 Numerical Modeling

The stress state within the gelatin blocks is described by the two parameters d and h (fig. 1a). We assume that the position and width, w , of the surface excavation are known exactly.

To calculate the elastic stresses within the gelatin, we use the two-dimensional (2D) Boundary Element (BE) code “*Cut&Displace*” (Crouch et al., 1983; Davis et al., 2017, 2019). Plane strain is assumed (the validity of this assumption will be discussed later).

The box bottom and walls are discretized into boundary elements of length $l_{BE} = 2$ mm. Displacement is set to zero on the bottom elements, while we impose fixed displacement on the side walls, equal to d or $-d$ (fig. 1) for extension or compression, respectively. The free surface is also discretized and BEs are shaped to model the excavation; stress boundary conditions are imposed on them to reproduce the gravitational stress due to the unload (Martel & Muller, 2000, eqs. 1).

We calculate the principal stress directions on a dense grid of observation points within the box. We simulate the crack trajectories assuming that the cracks open against, and propagate perpendicular to, the least compressive stress axis σ_3 (Anderson, 1951). This assumption makes a good approximation of real trajectories provided the size and volume of the cracks are not too large (Watanabe et al., 2002; Maccaferri et al., 2019) and the effects of its viscosity can be neglected, as well as those of stress gradients (Dahm, 2000), and that the cracks are not misaligned to the principal stress axes at the injection point. The more these assumptions are far from reality, the larger the mismatch between real and σ_3 -perpendicular trajectories. These factors can be accounted for by using more complex dike trajectory models, in 2D (Dahm, 2000; Maccaferri et al., 2011) and recently also in three dimensions (3D) (Davis et al., 2020), but since they would increase the number of parameters, larger data sets would be needed to perform a stress inversion.

2.4 MCMC Scheme

Our sampling procedure relies on the Delayed Rejection and Adaptive Metropolis (DRAM) MCMC algorithm (Haario et al., 2006; Laine, 2013). The set of N observed arrivals (x_i^{obs} , $i = 1, \dots, N$) is first divided into two subsets N^I and N^F ("I" and "F" stand respectively for "inversion" and "forecast"). The N^I set is used to sample the two parameters d and h . The size of the data sets we used varies from a minimum $N^I = 2$ in 2DLA-2 to a maximum of $N^I = 5$ in 2DLA-6 & 2DLA-7 (table 2).

At start, ranges and guesses for the parameters d and h are fixed together with a common starting depth for the cracks, $z_i^{start} = z^{start}$, shallower than the injection depth so that the cracks have some space to align perpendicularly to σ_3 (fig. 1). Starting locations x_i^{start} are then assigned as the horizontal coordinate of the upper tips of the observed cracks at z^{start} . At each iteration, we simulate N^I crack trajectories and sample d and h in order to minimize the objective function

$$S = \sum_{i=1}^{N^I} (x_i^s - x_i^{obs})^2 \quad (2)$$

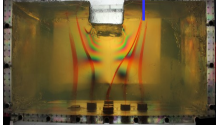
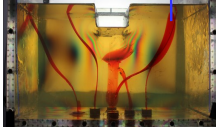
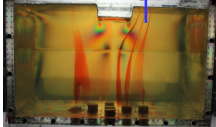
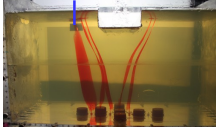
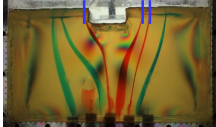
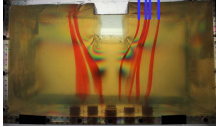
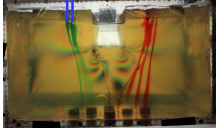
where x_i^s are the simulated arrivals.

The squares of the uncertainties on the two parameters ($\Delta d = \pm 0.1$ mm; $\Delta h = \pm 1$ mm) populate the diagonal of the covariance matrix (which is assumed diagonal). $M = 10^4$ iterations were made for every chain, with a burn-in time of 10^3 iterations. Our runs highlight a correlation between d and h , as expected from Rivalta et al. (2019), so we consider a further parameter: $R = \frac{d}{h}$, which partly removes the trade-off, and use the posterior probability distributions (PPDs) of d and R to perform the forecasts.

2.5 Forecasting Approach

After performing the inversions, we run $M^F = 10^3$ iterations of N^F simulations for the forecasts, where we sample the parameters (d , R) from their PPDs. Starting points are drawn from a Gaussian distribution centered on the observed ones, $x_i^{start,F}$, $z_i^{start,F}$,

Table 1. Experiments and measured parameters. Blue markers in the pictures indicate the arrivals used for the forecast (see fig. 2). Column 7: "t" = top; "b" = bottom layers. Updated d^{exp} and h^{exp} are indicated in parentheses.

# Exp.	Picture	H ± 1 mm	h^{exp} ± 1 mm	w ± 1 mm	d^{exp} ± 0.1 mm	E Pa	z^{start} ± 1 mm
2DLA-1		190	50	70	2.5	2930 ± 120	-100
2DLA-2		210	44	60	-2.5	2740 ± 130	-100
2DLA-3		217	21	70	2.5	t: 3150 ± 110 b: 5250 ± 460	-150
2DLA-4		195	24	70	2.5	t: 2300 ± 70 b: 2620 ± 400	-150
2DLA-5		196	24	70	0 (2.5)	2800 ± 70	-150
2DLA-6		219	58 (28)	60	2.5	2480 ± 50	-150
2DLA-7		219	72 (32)	60	2.5	2800 ± 60	-150
2DLA-8		210	55	60	-2.5	2700 ± 80	-100
2DLA-9		195	44	60	-2.5	2700 ± 80	-100
2DLA-10		195	30	70	-2.5	2960 ± 90	-100

with standard deviation $\sigma = 1 \text{ mm}$. The combined distribution of simulated arrivals is compared to the observed arrivals set aside for the forecast $x_i^{obs,F}$.

A different approach is adopted in experiments 2DLA-5 and 2DLA-6 & 2DLA-7 to account for the modified state of stress between the N^I and N^F cracks. In 2DLA-5 we fit the PPDs of d and R with Beta functions and then update them by shifting the mean value and their upper and lower limits to account for the added extension. In 2DLA-6 & 2DLA-7 we use the same strategy, except that we update h and R .

3 Results

3.1 Parameters sampling

We observe that, as expected, extension competes against surface unloading and leads to more vertical crack trajectories. This is clearly observed in 2DLA-5 and in 2DLA-6&7, where extension was applied and unloading was decreased midway through the experiment, respectively (compare green to red trajectories in table 1, 2DLA-5 and 2DLA-7).

In general, we find that our trajectory simulations for the experiments with extension are closer to the observations than those for the compressional cases, where the trajectories tend to diverge significantly from each other and spread the uncertainty of the initial location into a more spread distribution of the arrival locations (see section 2.2). This is reflected on the PPDs, which are generally spread and fail to recover the imposed values of the parameters in the only compressional case we performed an inversion on (2DLA-2).

In the homogeneous extensional cases, the PPDs for d and especially h are generally poorly constrained, though the imposed value d^{exp} is well recovered in 2DLA-5 and 2DLA-6 & 7, where it falls at the 44th and 45th percentile, respectively. In contrast, the PPD for R is always peaked around or close to R^{exp} (fig. 2). The distributions of h tend to be generally uniform. The PPDs, including those of h , are more peaked when more data are available (2DLA-6&7). In the layered cases (2DLA-3 and 2DLA-4), the medians of all the PPDs are rather far from the respective imposed values, except for R in 2DLA-4.

The joint distribution for R and h (fig. 2a) shows that R is generally well constrained while h is not.

3.2 Forecasts

We find that, in spite of the PPDs for d and h being often spread or even uniform, the forecast distribution always shows N^F sharp peaks. Moreover, in spite of the PPDs for d and h failing to accurately recover the imposed values, the peaks of the forecast distribution generally coincide or are very close to the observed arrivals (fig. 2b, table 2). This includes the layered cases. Again, the compressional case marks an exception: the forecast shows two maxima, one closer to the box center and a sharp one at the box margin (fig. 2b); this is due to the fact that many simulated cracks ended up hitting the right side of the box. Neither of the maxima coincides with the observed arrival, although the median does (fig. 2b, table 2).

Two secondary peaks are also obtained in the combined forecast distribution for 2DLA-5, as the sampling range for d allowed for both positive (extension) and negative (compression) values. The two main maxima are here close to the box center and show good agreement with $x_i^{obs,F}$. Considering the single distributions separately, the three $x_i^{obs,F}$ fall between the 47th and the 79th percentile. In 2DLA-6&7 ($N^F = 6$) three clear maxima are observed in the combined forecast distribution, showing again good agree-

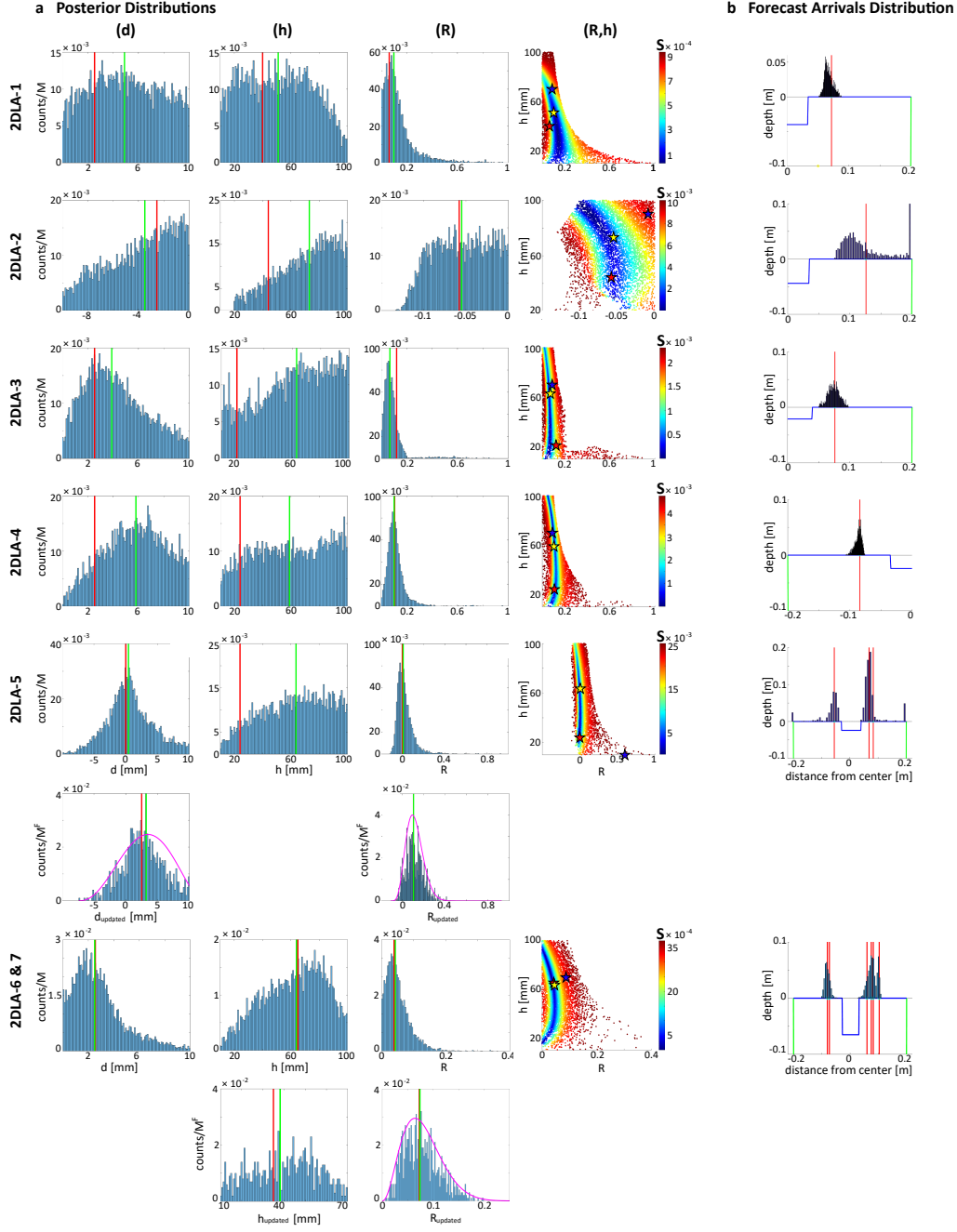


Figure 2. Summary of inversion and forecast results of the experiments reported in table 1. **a:** PPDs for parameters d , h and R and joint PPD for (R, h) . Red lines show the measured values; green lines the medians (table 1). The Beta functions used to fit and update the distributions in 2DLA-5 and 2DLA-6&7 are plotted in magenta. Last column from left: the starting guess, measured and median values are represented, respectively, by a blue, red and yellow star. The color palette shows the value of S for every sampled point in the parameters space, from dark red (higher S) to blue (lower S). **b:** countings of forecast arrivals displayed on a scheme of the box. Positions of the observed arrivals $x_i^{obs, F}$ are marked with red lines.

Table 2. Additional results from inversions and forecasts

Experiment code	N^I	N^F	$d^{exp} \pm 0.1$	d^{med}	$h^{exp} \pm 1$	h^{med}	$R^{exp} (\times 10^{-3})$	$R^{med} (\times 10^{-3})$	Forecast percentile
2DLA-1	4	1	2.5	4.9	50	51	63 ± 4	100	75
2DLA-2	2	1	-2.5	-3.5	44	73	-57 ± 4	-55	61
2DLA-3	3	1	2.5	3.9	21	63	120 ± 10	69	56
2DLA-4	4	1	2.5	5.8	24	59	104 ± 8	102	60
2DLA-5	3	3	0	0.4	24	64	$0 \pm 1 \times 10^{-2}$	8×10^{-3}	47*
									58*
									79*
2DLA-6 & 7	5	6	2.5	2.5	65	64	43 ± 2	39	51*
									77*
									35*
									44*
									34*
60*									

* Relative to the forecasts for each of the N^F arrivals in 2DLA-5, 6 & 7.

** After the stress update.

ment with the $x_i^{obs,F}$, which fall between the 34th and the 77th percentile of the respective individual distributions (table 2).

In all experiments with $N^F = 1$, the observed arrivals $x^{obs,F}$ fall between the 50th and the 75th percentiles (table 2).

4 Discussion and Conclusions

4.1 Method Validation

The inversion and forecast strategy we applied to our experimental data proved generally effective in retrieving information on the stress state within the gelatin blocks and very effective in identifying high-probability regions for crack arrivals on the surface (table 2). Forecasts are successful in spite of the sampling being carried out on scarce data sets. If data sets are larger (5 data points for 2 parameters), also the state of stress is recovered accurately. The method performs well also when the layering of the medium is neglected in the model. The same holds true for all the other inhomogeneities we neglected, such as previous cracks and local stress concentrations. Elastic parameters, if unknown, could be constrained through a similar sampling procedure, but information on the stress state would be necessary as they trade off. To test this possibility, we ran an inversion on the N^F data set of 2DLA-5, fixing both d and h as known parameters and inverting for E . We found the sampled E distribution peaks very close to E^{exp} (table 1), which falls at the 37th percentile of the distribution.

The forecast strategy applied in experiments 2DLA-5 and 2DLA-6&7 also proved effective in accounting for the modification of the stress field over time, validating the evolving-stress forecast method by Rivalta et al. (2019).

4.2 Limitations

A critical issue is the nearly-uniform trend observed in the PPDs for h , which leads to the "banana-shaped" joint distributions retrieved from the inversions (fig. 2a). This behavior arises from the fact that very shallow or very deep surface unloads, for the same d and starting points, lead to similar arrivals. We saw this effect both in the numerical simulations and in a separate experiment where two cracks were injected in a block with a deep surface excavation ($w = 7$ cm, $h = 10$) cm. Based on this, we conclude that the effect is due to the relaxation of the surface excavation's walls under gravity. This refocuses trajectories towards the center of the unload once, after having been deflected by the unloading, they approach the surface.

The method performs better with extensional rather than compressional settings. Several factors may contribute to this. Compressing gelatin blocks without inducing local stress concentrations proved difficult, and the crack trajectories were greatly affected by these. Both unloading and compression lead to more horizontal σ_1 directions within the medium. Thus, the mismatch between the crack orientation and the principal stress axes right after the injection is larger and the cracks need to cover longer distances before aligning to them. Moreover, a horizontal σ_1 may encourage cracks to propagate towards the back or the front walls of the box, thus making our 2D model unfit. Compressional settings may be inherently more challenging to forecast: trajectories tend to diverge, especially in case of unloading, and simulations are therefore more sensitive to any variability of initial and boundary conditions or model parameters.

4.3 Application to natural cases

Our results suggests that reliable forecasts of vent distribution can be carried out even with scarce data or a lack of knowledge of the layering structure of the host medium, as is often the case in nature. A stress field evolving with time can be approached with a distribution updating strategy.

The two parameters determining the state of stress in our model, d and h , play the role of tectonic and topographic load/unload stress in a natural case, respectively. Roman and Jaupart (2014) have shown that these two are in general the main contributions to elastic stresses at and beneath a volcano. They dominate over magma chamber pressurization stress because the latter is only significant very close to the magma reservoir (Roman & Jaupart, 2014). However, when these stresses are small (e.g., in the presence of a gently sloping topography or far away from plate margins), buoyancy can play a big role in driving dike propagation and should be accounted for.

An upgrade to three-dimensional modeling is necessary before application to volcanic regions to account for any geometry and topography-related effects.

Acknowledgments

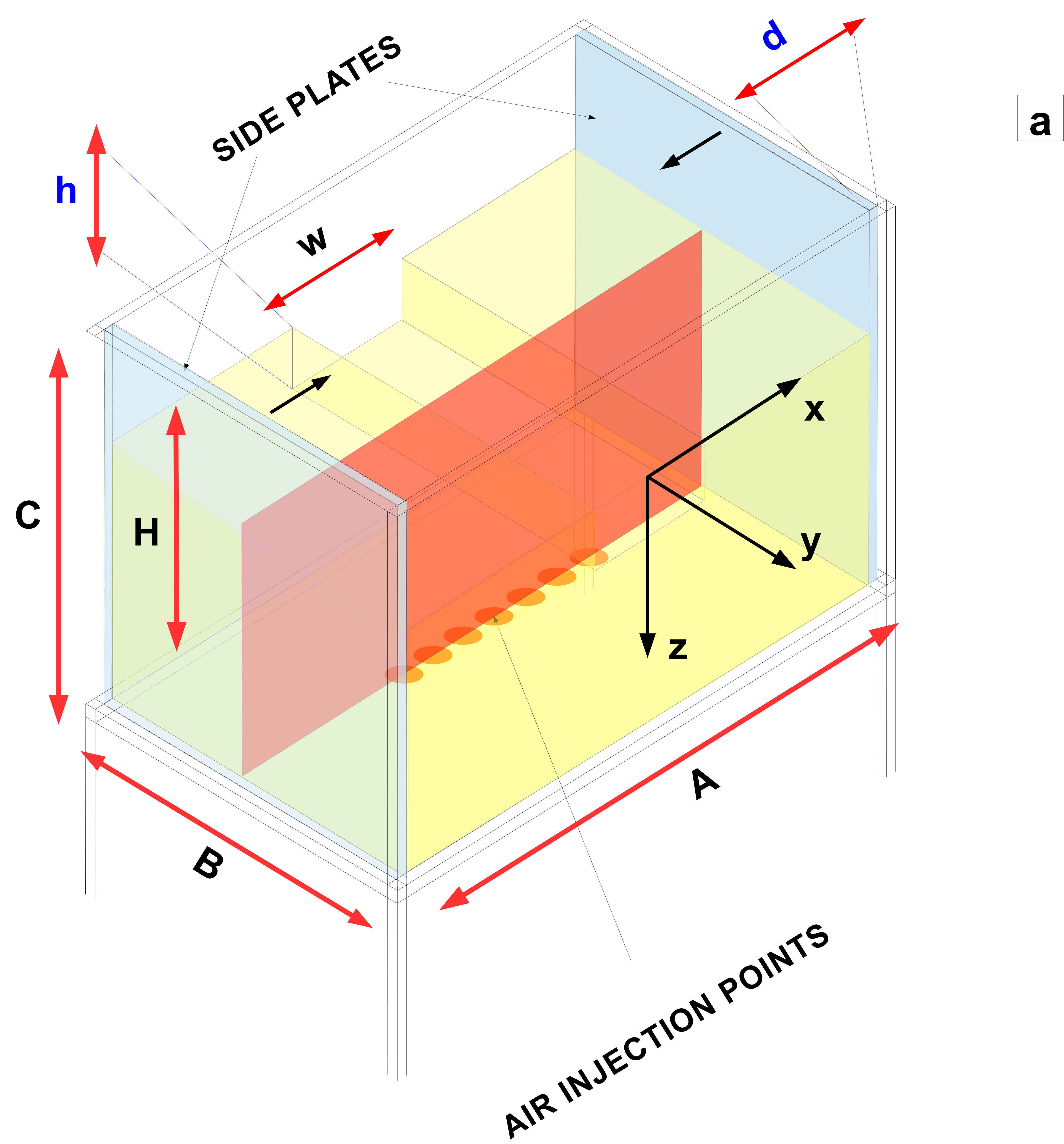
All data collected and used in this work are available under request. L.M. and T.D. are funded by the DFG grants N. RI 2782/6-1—ZO 277/3-1 and DFG-ICDP N. RI 2782/3-1, respectively. The numerical model is based on the open source code <https://doi.org/10.5281/zenodo.3694164>.

References

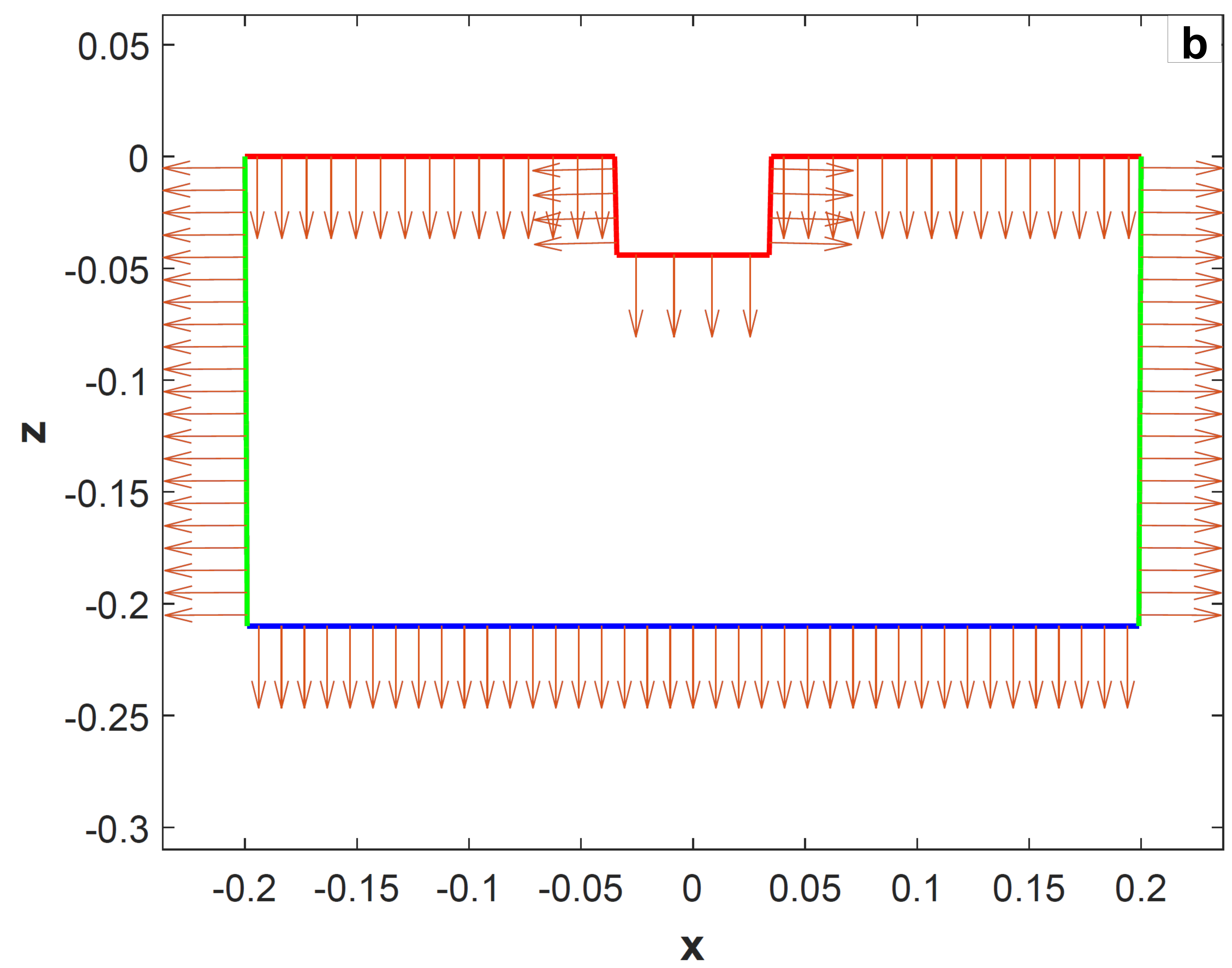
- Acocella, V., & Tibaldi, A. (2005). Dike propagation driven by volcano collapse: a general model tested at Stromboli, Italy. *Geophysical Research Letters*, *32*(8). doi: 10.1029/2004GL022248
- Anderson, E. M. (1951). *The dynamics of faulting and dyke formation with applications to Britain*. Hafner Pub. Co.
- Bevilacqua, A., Isaia, R., Neri, A., Vitale, S., Aspinall, W. P., Bisson, M., ... others

- (2015). Quantifying volcanic hazard at campi flegrei caldera (italy) with uncertainty assessment: 1. vent opening maps. *Journal of Geophysical Research: Solid Earth*, *120*(4), 2309–2329. doi: 10.1002/2014JB011775
- Connor, C. B., & Hill, B. E. (1995). Three nonhomogeneous poisson models for the probability of basaltic volcanism: application to the yucca mountain region, nevada. *Journal of Geophysical Research: Solid Earth*, *100*(B6), 10107–10125. doi: 10.1029/95JB01055
- Crouch, S. L., Starfield, A. M., & Rizzo, F. (1983). Boundary element methods in solid mechanics.
- Dahm, T. (2000). Numerical simulations of the propagation path and the arrest of fluid-filled fractures in the earth. *Geophysical Journal International*, *141*(3), 623–638. doi: 10.1046/j.1365-246x.2000.00102.x
- Davis, T., Healy, D., Bubeck, A., & Walker, R. (2017). Stress concentrations around voids in three dimensions: The roots of failure. *Journal of Structural Geology*, *102*, 193–207. doi: 10.1016/j.jsg.2017.07.013
- Davis, T., Healy, D., & Rivalta, E. (2019). Slip on wavy frictional faults: Is the 3rd dimension a sticking point? *Journal of Structural Geology*, *119*, 33–49. doi: 10.1016/j.jsg.2018.11.009
- Davis, T., Rivalta, E., & Dahm, T. (2020). Critical fluid injection volumes for uncontrolled fracture ascent. *Geophysical Research Letters*, e2020GL087774. doi: 10.1029/2020GL087774
- Gaete, A., Kavanagh, J. L., Rivalta, E., Hazim, S. H., Walter, T. R., & Dennis, D. J. (2019). The impact of unloading stresses on post-caldera magma intrusions. *Earth and Planetary Science Letters*, *508*, 109–121. doi: 10.1016/j.epsl.2018.12.016
- Haario, H., Laine, M., Mira, A., & Saksman, E. (2006). Dram: efficient adaptive mcmc. *Statistics and computing*, *16*(4), 339–354.
- Kavanagh, J., Menand, T., & Daniels, K. A. (2013). Gelatine as a crustal analogue: Determining elastic properties for modelling magmatic intrusions. *Tectonophysics*, *582*, 101–111. doi: 10.1016/j.tecto.2012.09.032
- Laine, M. (2013). Mcmc toolbox for matlab, 2013. URL: <http://helios.fmi.fi/~lainema/mcmc>.
- Maccaferri, F., Bonafede, M., & Rivalta, E. (2010). A numerical model of dyke propagation in layered elastic media. *Geophysical Journal International*, *180*(3), 1107–1123. doi: 10.1111/j.1365-246X.2009.04495.x
- Maccaferri, F., Bonafede, M., & Rivalta, E. (2011). A quantitative study of the mechanisms governing dike propagation, dike arrest and sill formation. *Journal of Volcanology and Geothermal Research*, *208*(1-2), 39–50. doi: 10.1016/j.jvolgeores.2011.09.001
- Maccaferri, F., Smittarello, D., Pinel, V., & Cayol, V. (2019). On the propagation path of magma-filled dikes and hydrofractures: The competition between external stress, internal pressure, and crack length. *Geochemistry, Geophysics, Geosystems*, *20*(4), 2064–2081. doi: 10.1029/2018GC007915
- Martel, S. J., & Muller, J. R. (2000). A two-dimensional boundary element method for calculating elastic gravitational stresses in slopes. *Pure and Applied Geophysics*, *157*(6-8), 989–1007. doi: 10.1007/s000240050014
- Martin, A. J., Umeda, K., Connor, C. B., Weller, J. N., Zhao, D., & Takahashi, M. (2004). Modeling long-term volcanic hazards through bayesian inference: An example from the tohoku volcanic arc, japan. *Journal of Geophysical Research: Solid Earth*, *109*(B10). doi: 10.1029/2004JB003201
- Menand, T., & Tait, S. R. (2001). A phenomenological model for precursor volcanic eruptions. *Nature*, *411*(6838), 678–680. doi: 10.1038/35079552
- Muller, J. R., Ito, G., & Martel, S. J. (2001). Effects of volcano loading on dike propagation in an elastic half-space. *Journal of Geophysical Research: Solid Earth*, *106*(B6), 11101–11113. doi: 10.1029/2000JB900461

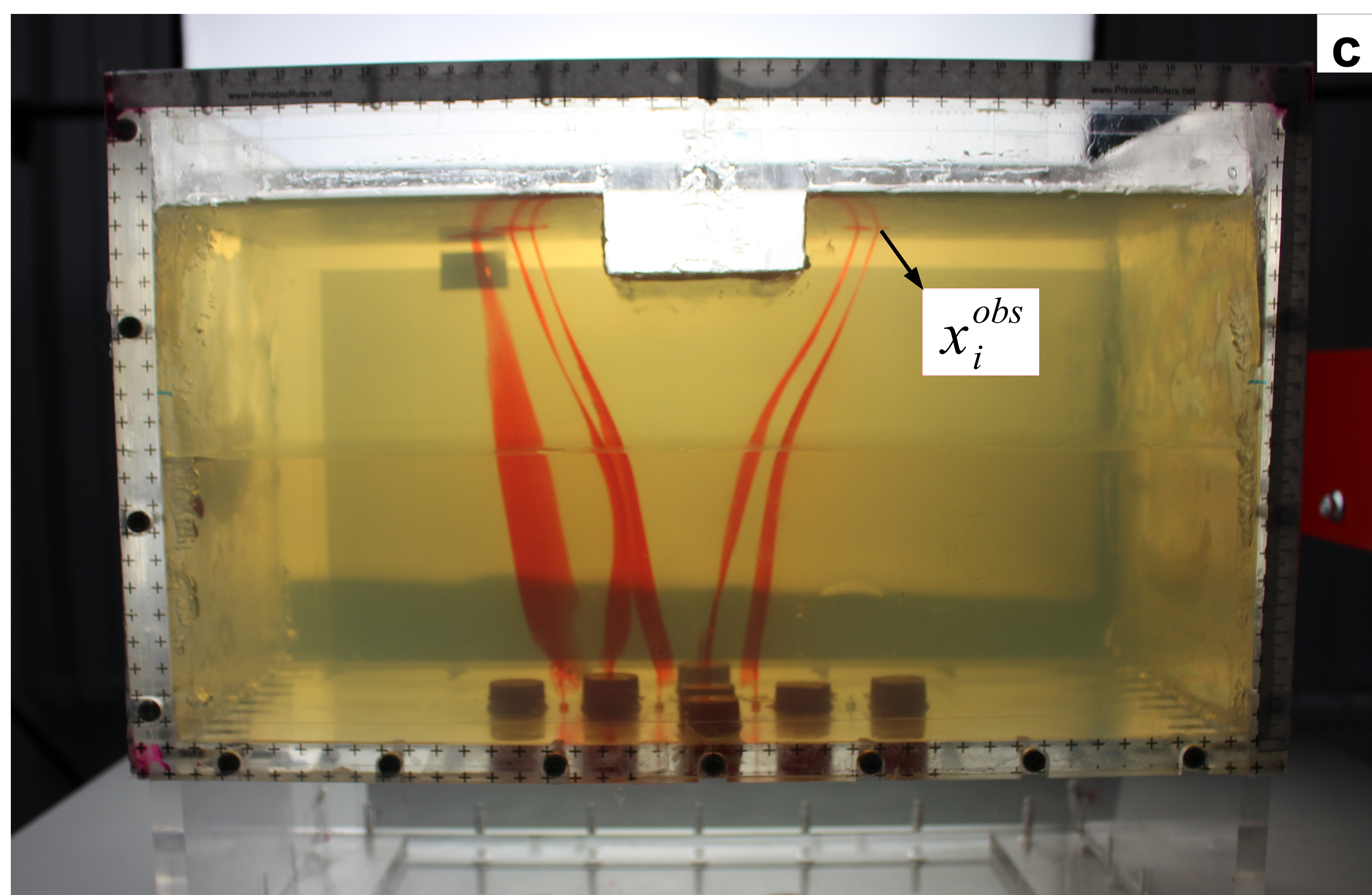
- Nakashima, Y. (1993). Buoyancy-driven propagation of an isolated fluid-filled crack in rock: implication for fluid transport in metamorphism. *Contributions to Mineralogy and Petrology*, *114*(3), 289–295. doi: 10.1007/BF01046532
- Rivalta, E., Corbi, F., Passarelli, L., Acocella, V., Davis, T., & Di Vito, M. A. (2019). Stress inversions to forecast magma pathways and eruptive vent location. *Science advances*, *5*(7), eaau9784. doi: 10.1126/sciadv.aau9784
- Roman, A., & Jaupart, C. (2014). The impact of a volcanic edifice on intrusive and eruptive activity. *Earth and Planetary Science Letters*, *408*, 1–8. doi: 10.1016/j.epsl.2014.09.016
- Selva, J., Orsi, G., Di Vito, M. A., Marzocchi, W., & Sandri, L. (2012). Probability hazard map for future vent opening at the campi flegrei caldera, italy. *Bulletin of volcanology*, *74*(2), 497–510. doi: 10.1007/s00445-011-0528-2
- Smittarello, D. (2019). *Propagation des intrusions basaltiques. modélisation analogique et suivi temporel par inversion des données de déplacements* (Unpublished doctoral dissertation). Université Grenoble Alpes.
- van Otterloo, J., & Cruden, A. R. (2016). Rheology of pig skin gelatine: Defining the elastic domain and its thermal and mechanical properties for geological analogue experiment applications. *Tectonophysics*, *683*, 86–97. doi: 10.1016/j.tecto.2016.06.019
- Watanabe, T., Masuyama, T., Nagaoka, K., & Tahara, T. (2002). Analog experiments on magma-filled cracks. *Earth, planets and space*, *54*(12), 1247–1261. doi: 10.1186/BF03352453



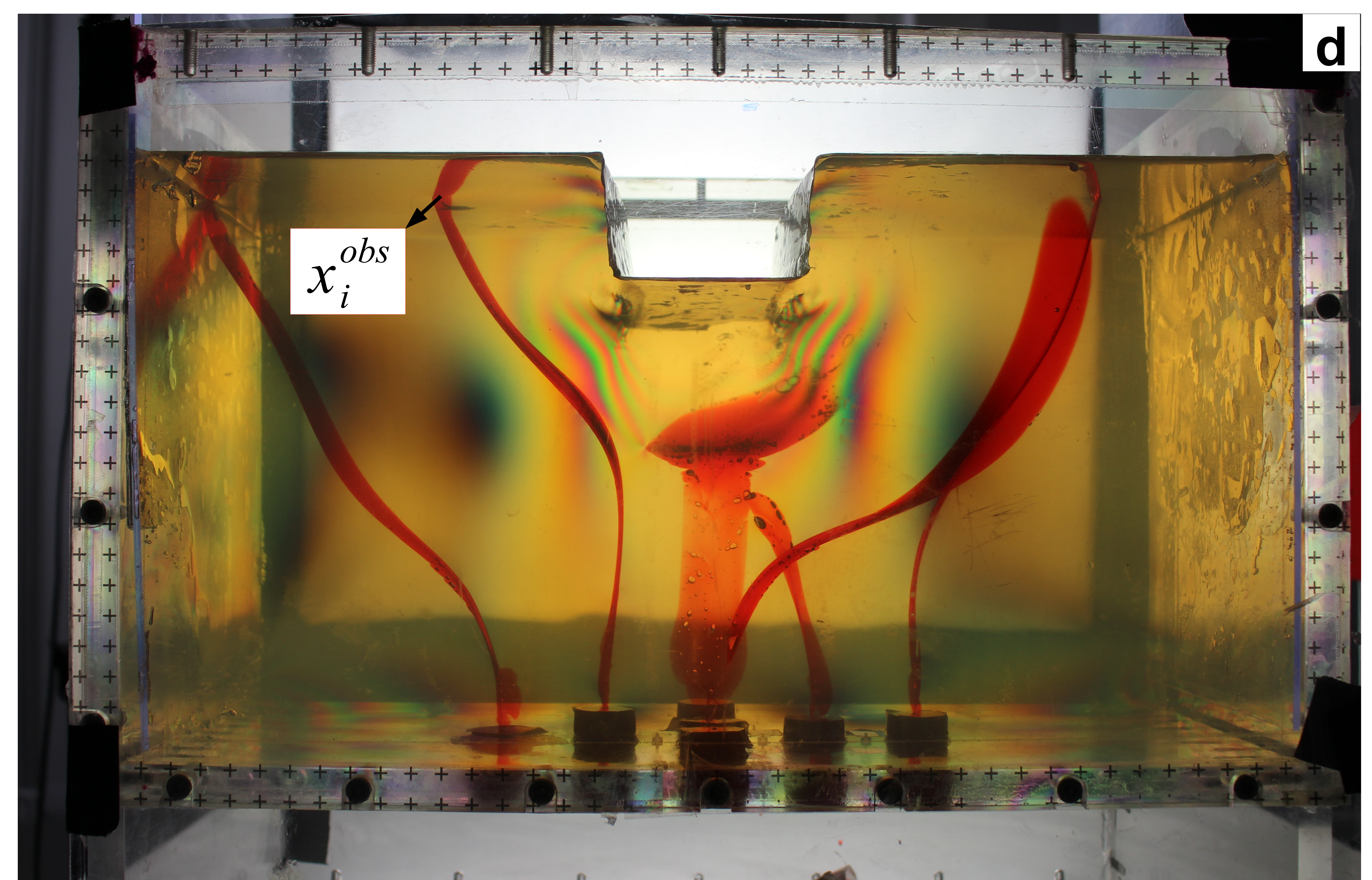
a



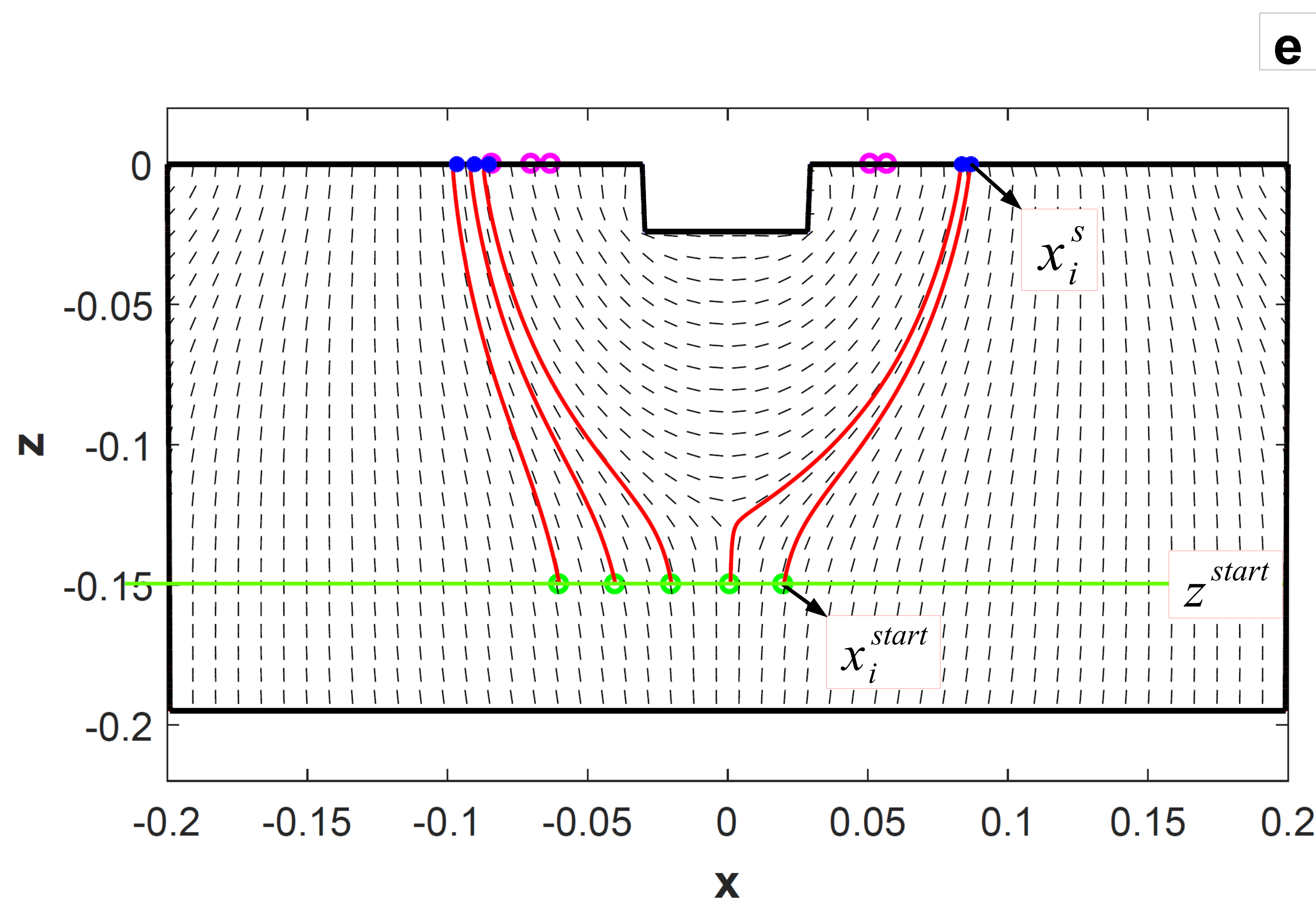
b



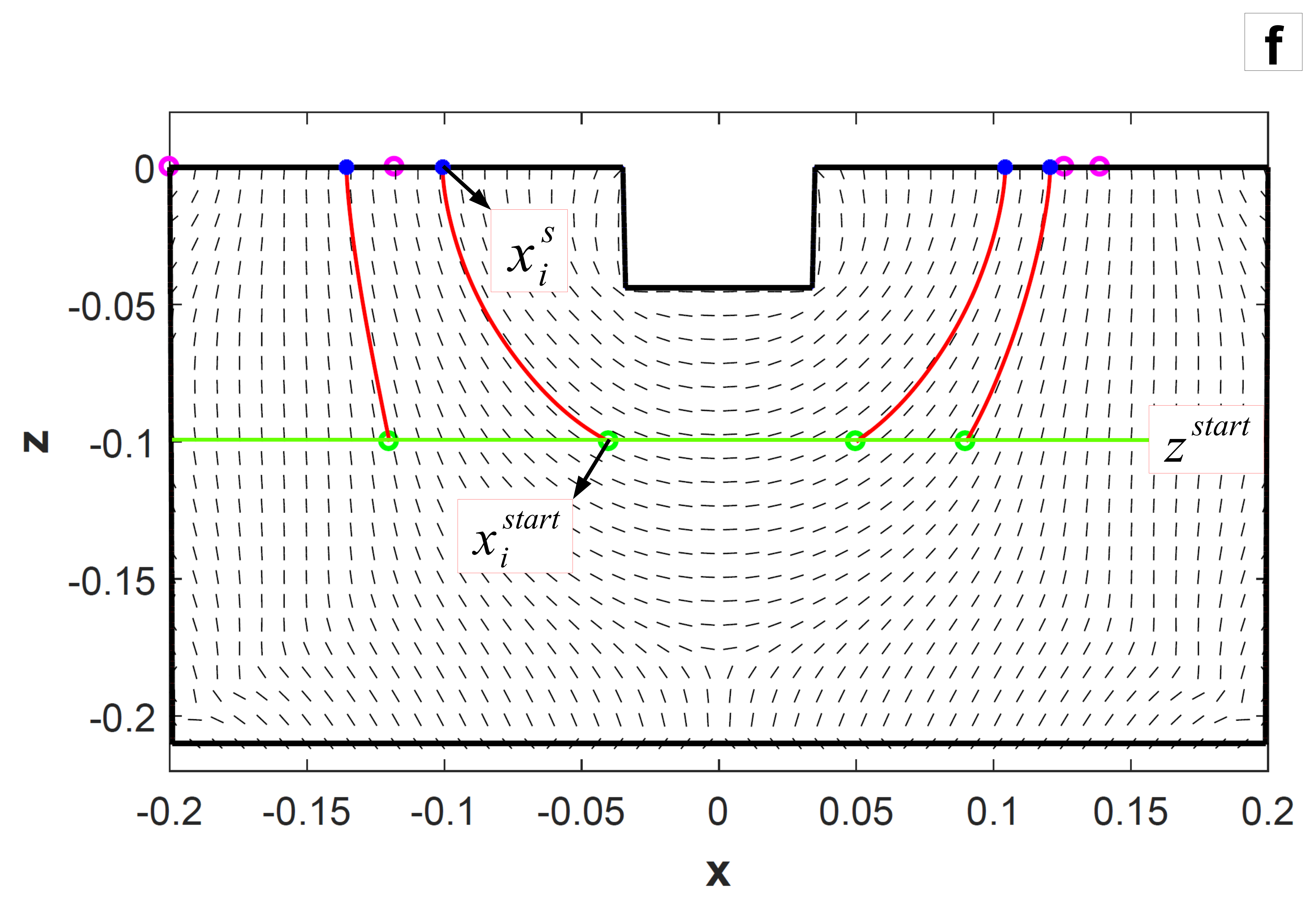
c



d

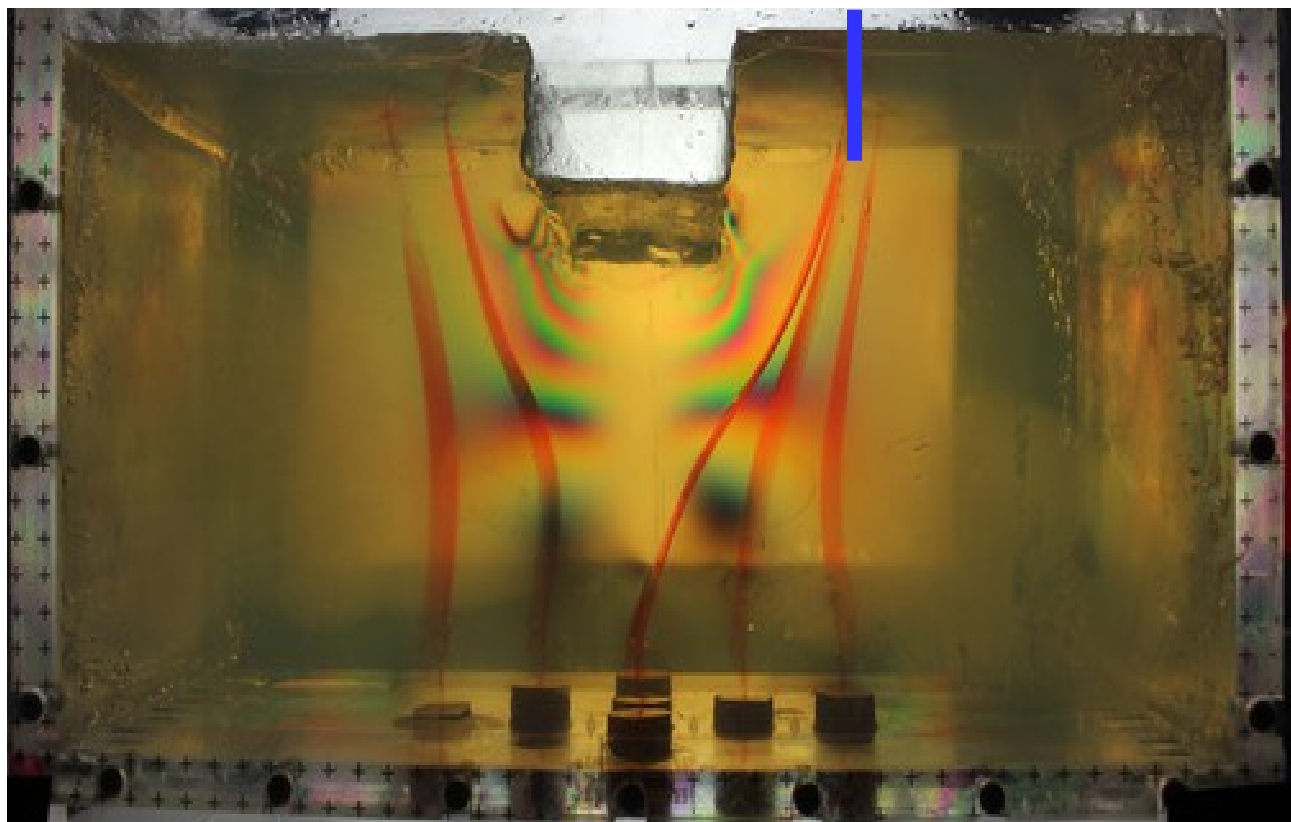


e

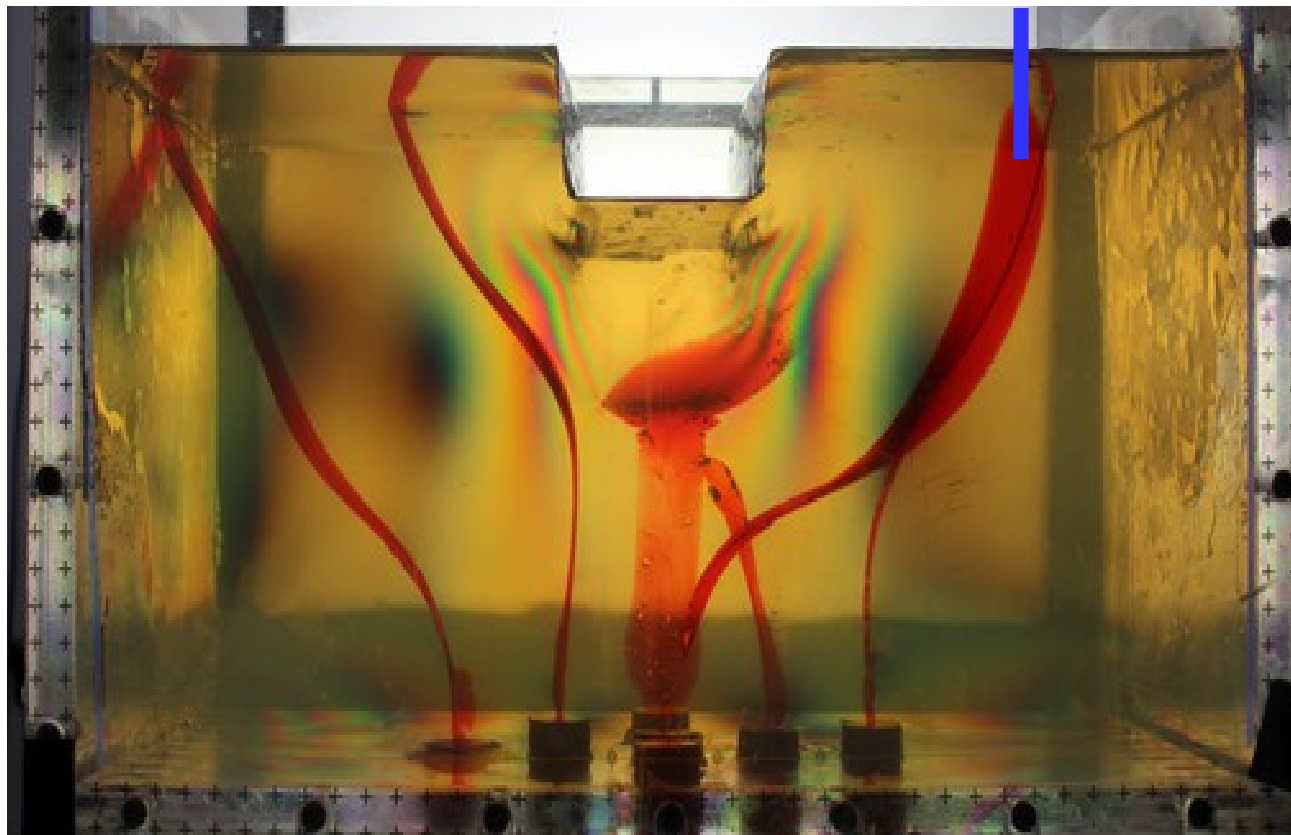


f

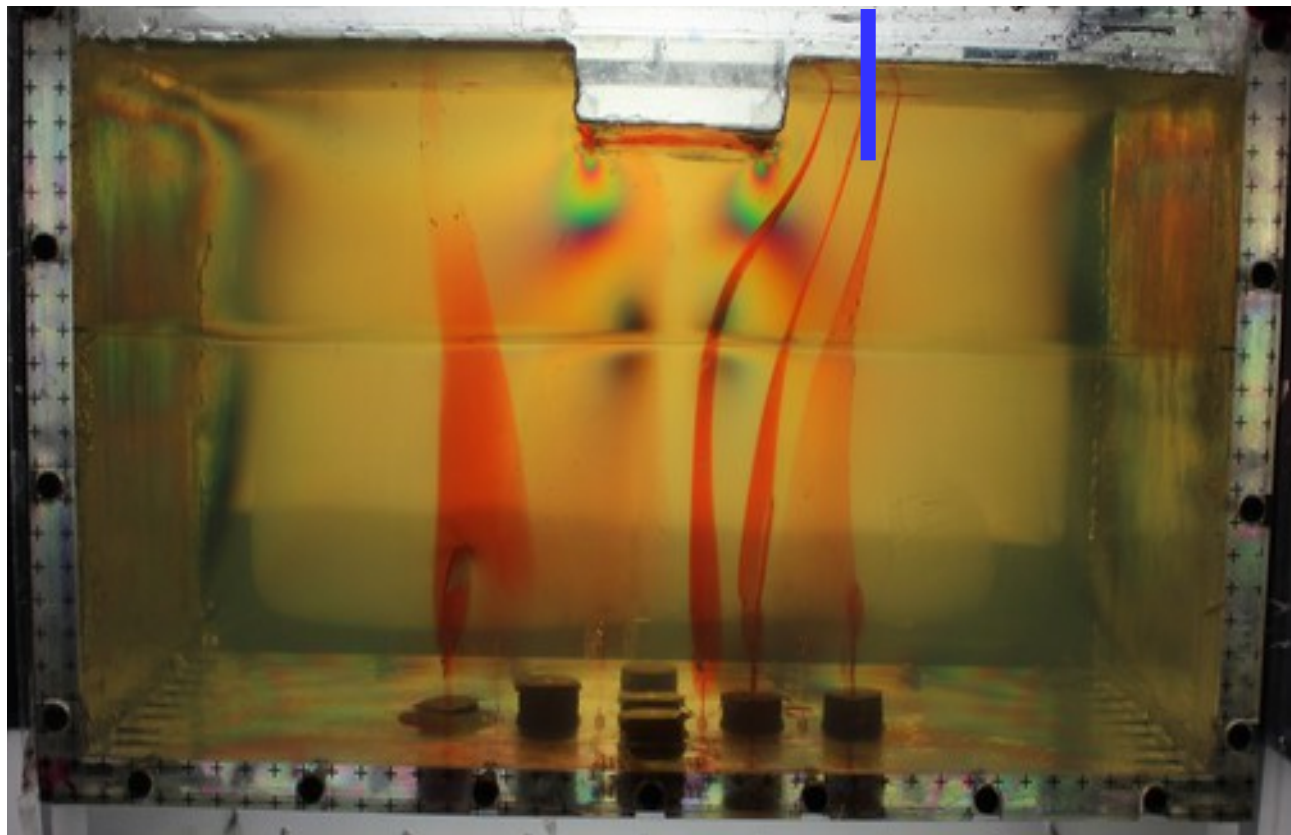
part of Table 1.



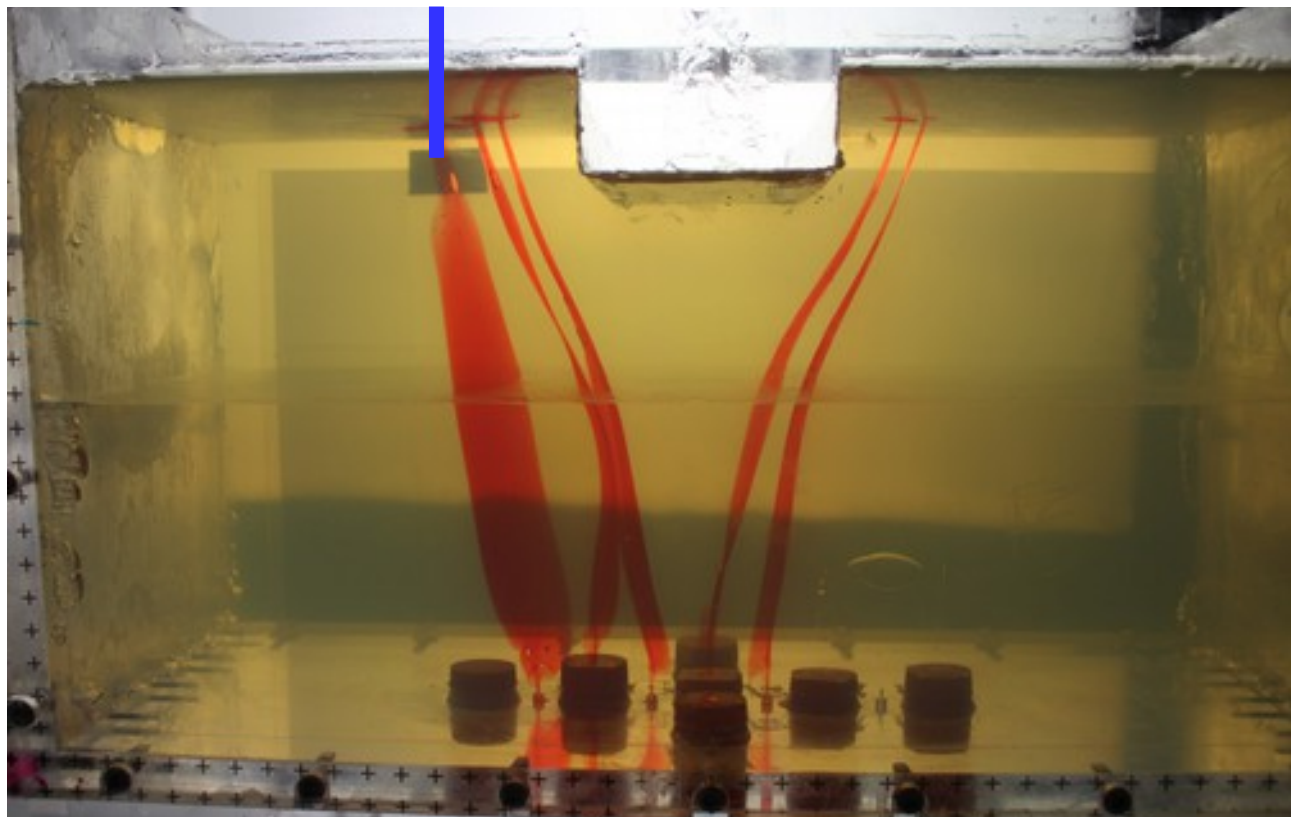
part of Table 1.



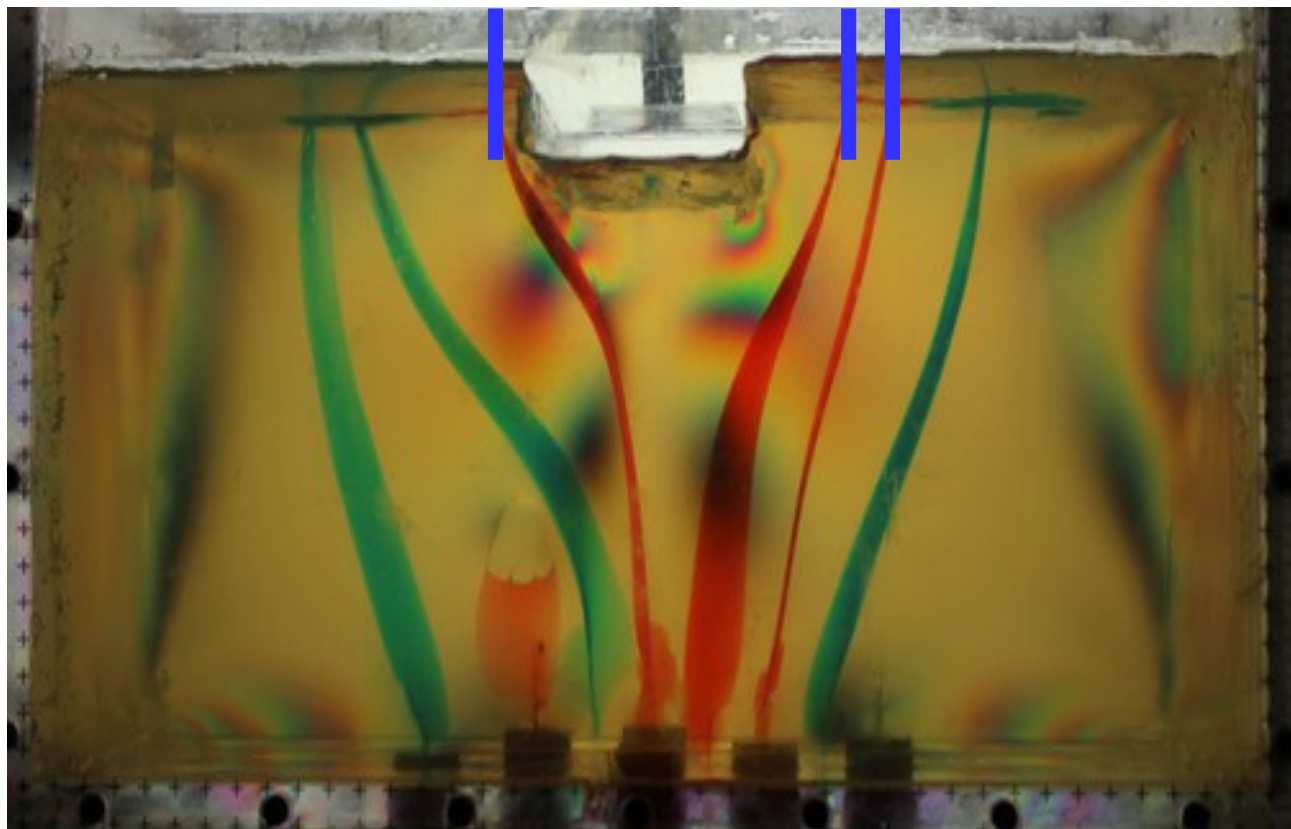
part of Table 1.



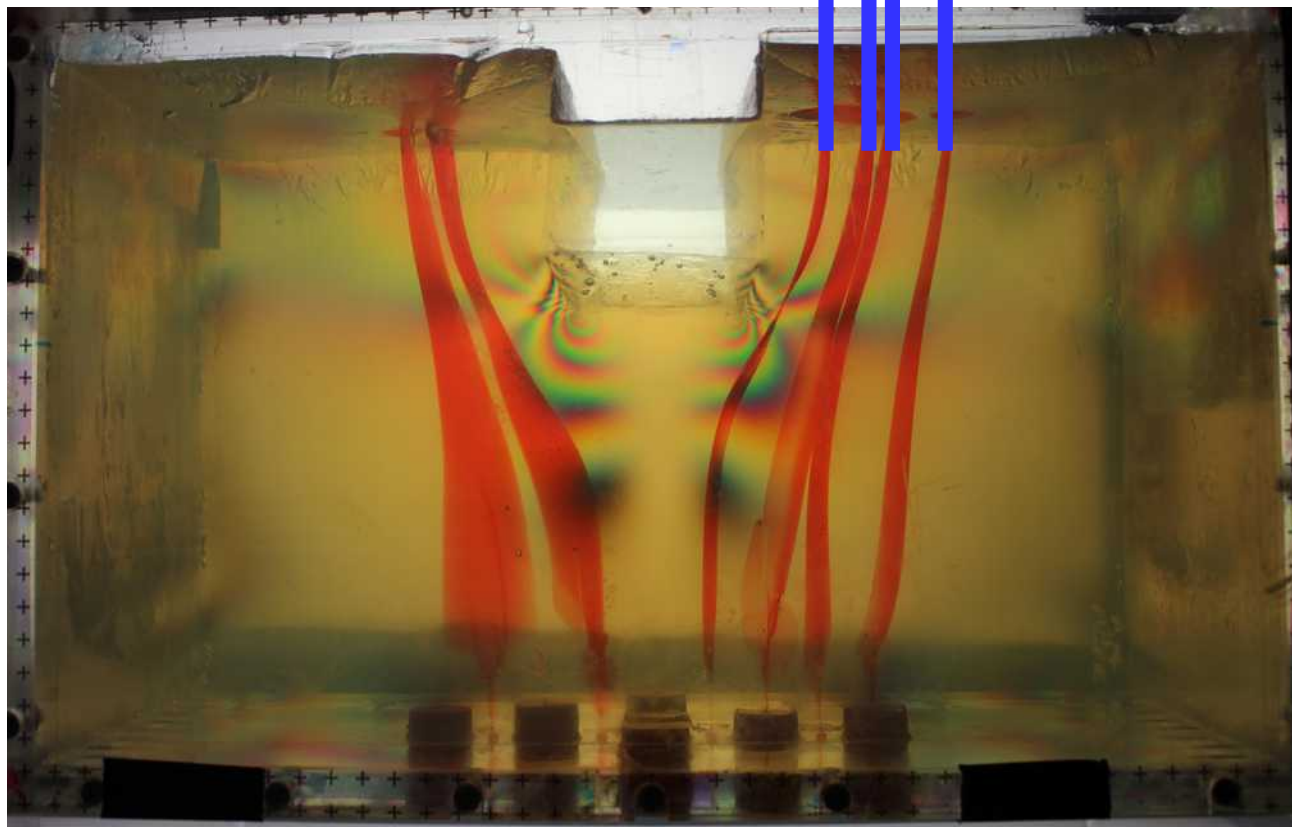
part of Table 1.



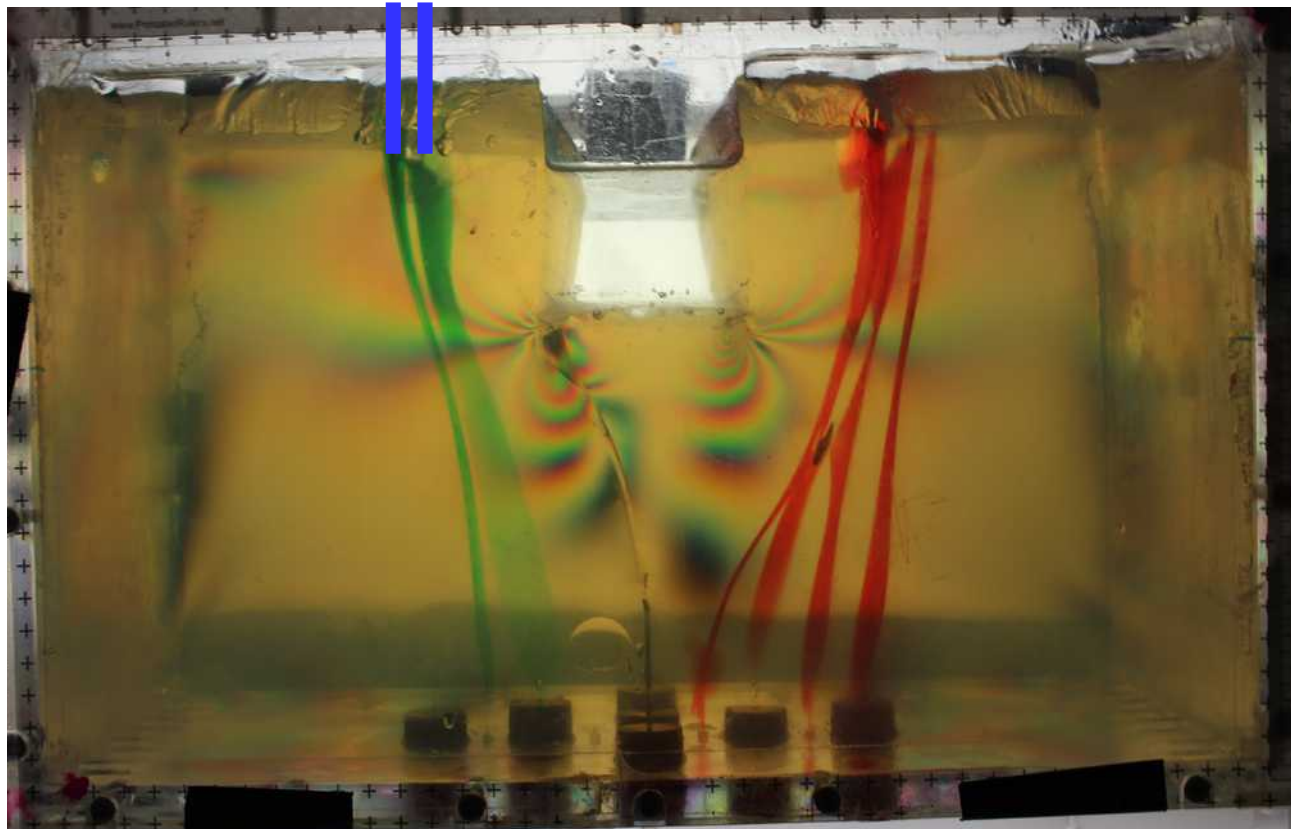
part of Table 1.



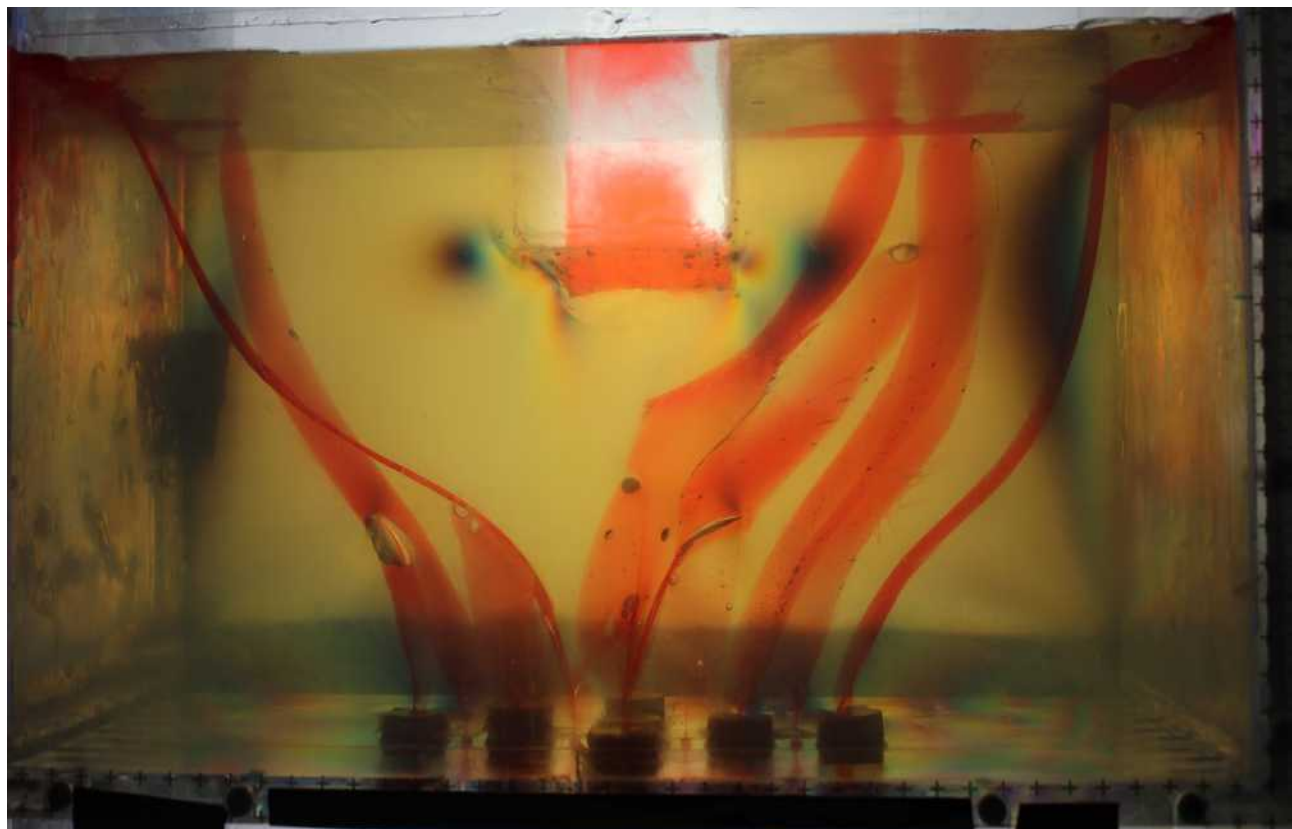
part of Table 1.



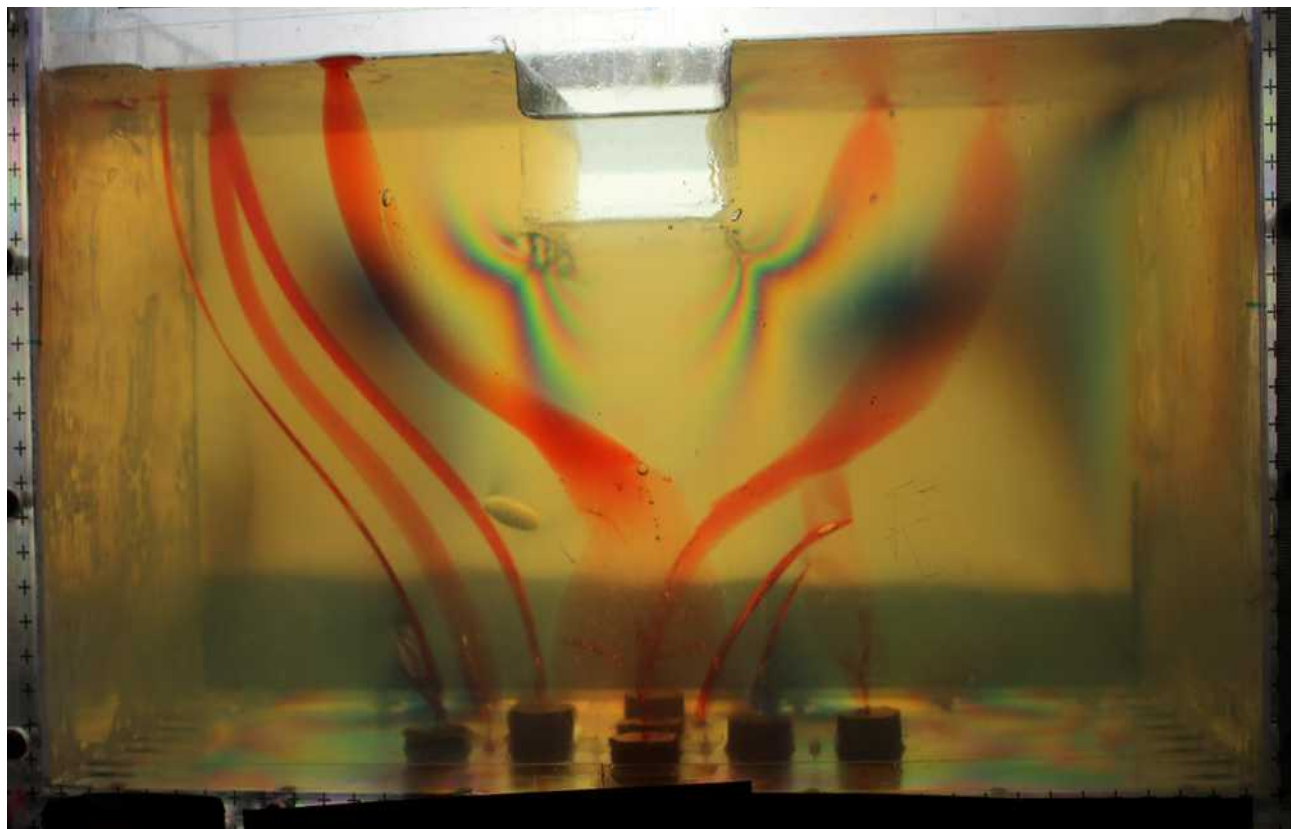
part of Table 1.



part of Table 1.



part of Table 1.



part of Table 1.

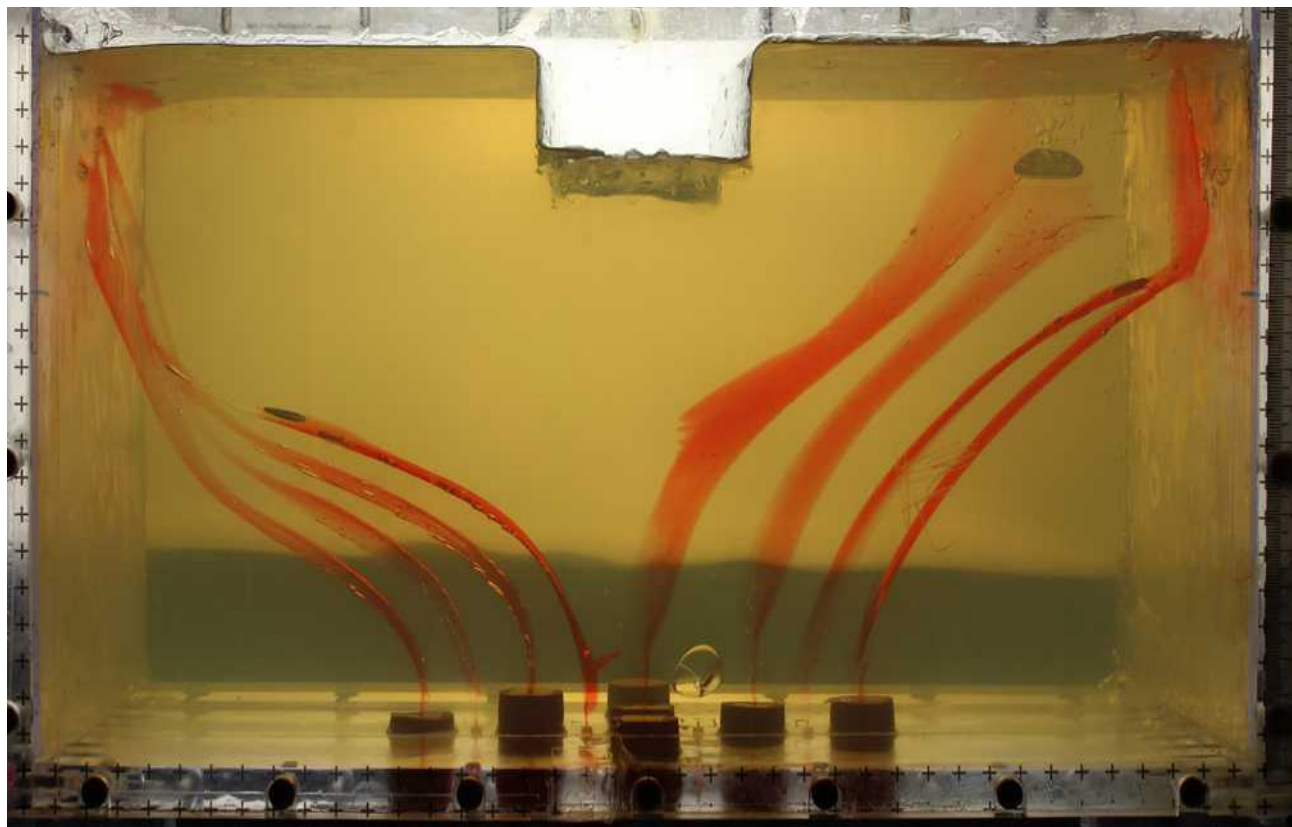


Figure 2.

